Ferromagnetism with Strong Perpendicular Magnetic Anisotropy in Epitaxial SrMn$_{0.3}$Ir$_{0.7}$O$_3$ Perovskite Films

Pengxiang Hou,[1] Yiren Liu,[2] Zhiyu Liu,[1] Chuanhui Zhu,[3] Yao Li,[1] Zhongnan Xi,[1] Yajie Han,[1] Jiayi Li,[1] Man-Rong Li,[3] Jian Zhou,[1] Lan Chen,[1,*] Yu Deng,[1] Yurong Yang,[1] Jun-Ming Liu,[2] and Di Wu[1,†]

[1]*National Laboratory of Solid State Microstructures, Collaborative Innovation Center of Advanced Microstructures, Jiangsu Key Laboratory of Artificial Functional Materials, and Department of Materials Science and Engineering, Nanjing University, Nanjing, 210093, People's Republic of China*

[2]*National Laboratory of Solid State Microstructures, Collaborative Innovation Center of Advanced Microstructures, and School of Physics, Nanjing University, Nanjing, 210093, People's Republic of China*

[3]*Key Laboratory of Bioinorganic and Synthetic Chemistry of Ministry of Education, and School of Chemistry, Sun Yat-Sen University, Guangzhou, 510275, People's Republic of China*

Strong Coulomb repulsion and spin-orbit coupling are known to give rise to exotic physical phenomena in transition metal oxides. Here, we report magnetic characteristics of a SrMn$_{0.3}$Ir$_{0.7}$O$_3$ perovskite thin film, having both $3d$ and $5d$ elements on the B sites, with a strong perpendicular magnetic anisotropy (PMA), which is rare in perovskite oxide thin films. The SrMn$_{0.3}$Ir$_{0.7}$O$_3$ films have been epitaxially deposited on (001)-oriented SrTiO$_3$ single-crystal substrates by pulsed-laser deposition, exhibiting a para-to-ferromagnetic transition at about 110 K. The average valence of Mn and Ir cations are estimated as $+3.61$ and $+4.17$, respectively, by x-ray photoelectron spectroscopy. X-ray absorption spectroscopy reveals that Mn e_g electrons occupy preferentially the $d_{3z^2-r^2}$ orbital, which produces the observed PMA in the framework of spin-orbital coupling. The SrMn$_{0.3}$Ir$_{0.7}$O$_3$ thin film shows a large effective anisotropy constant of about 1.2×10^6 erg cm^{-3} at 10 K, which is found to decrease with decreasing tetragonality c/a of the film. First-principles calculations reveal that Mn and Ir cations provide opposite magnetizations in SrMn$_{0.3}$Ir$_{0.7}$O$_3$ and the Mn e_g orbital polarization comes from both lattice distortion and oxygen octahedron rotation. The SrMn$_{0.3}$Ir$_{0.7}$O$_3$ thin film with strong PMA may have applications in future low-power-consumption oxide spintronic devices.

I. INTRODUCTION

Perovskite oxides in the form ABO$_3$ have been studied extensively for all-oxide spintronic applications [1]. The coexistence and competition between strong electron correlation and strong spin-orbit coupling (SOC) by combining $3d$ and $5d$ elements have attracted much attention due to their rich physical properties in $3d/5d$ oxide films, such as current-induced magnetization switching, topological Hall effect, and uniaxial magnetic anisotropy [2–4]. Among these properties, magnetic anisotropy is useful in both fundamental physics and alternative spintronic applications. In particular, thin films with the magnetic moments preferentially pointing perpendicular to the film plane, i.e., with the perpendicular magnetic anisotropy (PMA), are essential for achieving high-density, high-stability, and low-power-consumption spintronic devices [5–8]. Furthermore, competition between PMA and other

mechanisms, such as the Dzyaloshinskii-Moriya interaction, leads to other spin textures, such as chiral domain walls, magnetic skyrmions, and other topological phenomena [9–11]. However, due to the strong demagnetization effect, the magnetic moments of ferromagnetic thin films tend to lie in plane [12]. It has been extensively studied to overcome demagnetization and stabilize the PMA in a variety of films and multilayers [13–15].

In perovskite oxide magnetic thin films and heterostructures, the magnetic anisotropy is determined by the SOC and the anisotropy of crystalline structure, including B—O bond length and bond angle [16,17]. Thus, the magnetic ground state is coupled to the structural degree of freedom and can be manipulated via structure changes by fine tuning the strain, especially in epitaxial thin films [18]. Recently, it is found that magnetic anisotropy in layered iridates can be largely affected by tetragonal distortion and oxygen octahedron rotation [19]. Lin *et al.* achieved switching the magnetic easy axis in SrRuO$_3$ thin films via controlling Ru—O bond angles by LaNiO$_3$ capping layers [20]. $5d$ elements with strong SOC have

———————
*chenlan@nju.edu.cn
†diwu@nju.edu.cn

also been reported to have a great influence on the magnetic characteristics in various films. For example, Lu *et al.* reported 5*d* heavy-metal oxides with strong SOC to enhance and tune the magnetic anisotropy in tricolor 3*d*/5*d* oxide superlattices [21]. Yi *et al.* reported that magnetic anisotropy in $La_{2/3}Sr_{1/3}MnO_3/SrIrO_3$ (LSMO/SIO) superlattices is associated with the strong SOC from Ir and can be controlled via interfacial oxygen octahedron rotation [22].

In this paper, we report magnetic characteristics of epitaxial $SrMn_{0.3}Ir_{0.7}O_3$ (SMIO) thin films deposited on (001)-oriented $SrTiO_3$ (STO) substrates. The SMIO films are ferromagnetic below about 110 K and exhibit a strong PMA with an effective anisotropy constant of about 1.2×10^6 erg cm^{-3} at 10 K. By depositing SMIO films on $BaTiO_3$ (BTO) buffer layers of various thickness, SMIO films with various tetragonality are achieved to deconvolute the effect of lattice distortion on the observed PMA. First-principles calculations confirm that both lattice distortion and oxygen octahedron rotation result in the observed strong PMA.

II. EXPERIMENTAL METHODS

A. Deposition of films

The SMIO films are deposited by pulsed-laser deposition. Before deposition, the (001)-oriented STO substrate is etched in a NH_4F buffered HF solution ($NH_4F/HF = 7$:1) for 45 s and annealed at 950 °C for 75 min in flowing O_2 to achieve a TiO_2-single-terminated surface. The SMIO target is prepared by pressing a desired amount of fully mixed Sr_2IrO_4 and MnO_2 powders under 3 GPa for 30 min at room temperature. The ablation is performed using a 248-nm KrF excimer laser (COMPex-Pro 205F, Coherent) with an energy flux density about 1.7 J/cm^2 on the target and a repetition rate of 2 Hz. The oxygen pressure in the chamber is kept at 0.1 mbar, while the substrate temperature is maintained at 650 °C for SMIO. The BTO buffer layers are deposited at 750 °C under 0.01-mbar O_2 pressure by ablating a ceramic target prepared by solid-state reaction. For comparison, the $SrMnO_3$ (SMO), LSMO, and SIO films are also deposited by pulsed-laser deposition on (001)-oriented STO substrates. The substrate temperature and the oxygen pressure are maintained at 650 °C and 0.1 mbar for SMO and LSMO, while those of SIO are kept at 750 °C and 0.1 mbar, respectively. All of the deposition is monitored *in situ* by reflection high-energy electron diffraction to ensure a layer-by-layer deposition.

B. Structural and magnetization characterizations

Surface morphology of the SMIO films is checked with an Asylum Research Cypher ES atomic force microscope. The crystallinity, thickness, and lattice constants of the films is measured on a Bruker D8 Discover X-ray diffractometer with Cu $K\alpha_1$ radiation ($\lambda = 1.54$ Å). Cross-section high-angle annular dark field (HAADF) STEM images are acquired using a FEI Titan3 G2 aberration-corrected transmission electronic microscope, operating at 300 kV. The samples are prepared using a Helios G4 CX (Thermo Fisher) focused ion-beam setup prior to STEM measurements. Magnetic measurements are carried out on a superconducting quantum interference device magnetometer (MPMS XL 7, Quantum Design).

C. X-ray photoemission spectroscopy and x-ray absorption spectroscopy measurements

X-ray photoemission spectroscopy (XPS) is employed at room temperature to evaluate the valence and composition using a Thermo Scientific K-Alpha spectrometer. X-ray absorption spectroscopy (XAS) measurements around the Mn *L* edge are collected at 80 K in total electron yield mode at beamline BL08U1A in Shanghai Synchrotron Radiation Facility, and beamlines MCD-A and MCD-B (Soochow Beamline for Energy Materials) at National Synchrotron Radiation Facility, China. X-ray line dichroism (XLD) spectra are measured with linearly polarized x-ray beams, incident by 0° and 60° to the film normal, respectively. The spectra intensity is normalized so that the L_3 pre-edge and L_2 postedge have identical intensities for the two polarizations and the XLD is calculated as the intensity difference.

D. First-principles calculations

First-principles calculations are performed within density-functional theory, as implemented in the Vienna *ab initio* simulation package [23–26]. An energy cutoff of 550 eV is used, and the set of projector-augmented wave potentials is employed to describe the electron-ion interaction. Valence electron configurations, $4s^24p^65s^2$ for Sr, $5d^86s^1$ for Ir, $3s^23p^63d^54s^2$ for Mn and $2s^22p^4$ for O are considered. Electronic relaxations converged within 10^{-7} eV and ionic relaxation is performed until the residual force is <1 meV/Å. We use the PBEsol $+ U +$ SOC functional (selecting $U = 2$ eV for the Ir and $U = 3$ eV for Mn) for electronic structure calculations [27]. Supercell containing $2 \times 2 \times 2$ ABO_3 unit cells with six Ir and two Mn cations on the *B* sites is used, and a Γ-centered $8 \times 8 \times 8$ *k*-point mesh is adopted.

III. RESULTS AND DISCUSSION

A. Structure characterizations

Figure 1(a) shows a ω–2θ x-ray diffraction (XRD) pattern of the SMIO film deposited on the STO substrate. Only (00*l*) diffraction peaks from the SMIO film and the substrate are observed, indicating a high crystalline quality with no observable secondary phases. The (002)

diffraction peak of SMIO at $2\theta = 45.50°$ corresponds to an out-of-plane lattice constant of 3.976 Å. The clear Kiessig fringes in the x-ray reflection pattern of the SMIO/STO heterostructure (see the Supplemental Material [28]) indicate a smooth SMIO surface and a sharp SMIO/STO interface. Thickness of the SMIO film is approximately 20 nm, acquired through fitting the Kiessig fringes [29]. Figure 1(b) shows the x-ray reciprocal space mapping around the (103) spot of the STO substrate. It is clear that the (103) reflection of the SMIO film shares the same in-plane reciprocal vector with the substrate, indicating that the film is coherently grown and fully strained to the substrate. With the in-plane lattice constant of 3.905 Å, tetragonality (c/a) of the SMIO film is about 1.018, exhibiting a clear tetragonal distortion. Figure 1(c) shows typical cross-section HAADF STEM images of the SMIO/STO heterostructure, recorded along the [010] zone axis. Since the contrast of a HAADF STEM image is proportional to the atomic number of the columns by Z^2, one can identify the atoms directly from the contrast. The SMIO layer shows an obvious brighter contrast than the STO substrate with a clear SMIO/STO interface. The right panel of Fig. 1(c) shows the intensity profile along the green arrow. The uniform intensity of the perovskite B sites indicates that Mn and Ir cations are distributed randomly in the SMIO film. The lattice spacings of SMIO obtained from the HADDF STEM images are 3.976 Å along [001] and 3.905 Å along [100], respectively, which are consistent with the XRD results, indicating again that the SMIO film is fully strained to the substrate. Figure 1(d) is a typical atomic force microscope (AFM) image of the SMIO

film surface, showing a clear step-and-terrace morphology in agreement with the layer-by-layer deposition. The SMIO film surface is smooth with the root-mean-square roughness less than 150 pm over a $3 \times 3 \ \mu m^2$ area. LSMO, SMO, and SIO films are all in high-quality epitaxy, as indicated by the XRD patterns shown in Fig. S4 within the Supplemental Material [28].

B. Magnetic characterizations

Figure 2(a) shows the in-plane and out-of-plane temperature-dependent magnetization (M–T) curves of the SMIO film. The sample is cooled in a 5-T magnetic field applied in plane (out of plane) and then measured during heating with a 0.1 T field applied in plane (out of plane). There is a clear paramagnetic-ferromagnetic phase transition in SMIO. The transition temperature is about 110 K, as estimated from the temperature-dependent magnetic susceptibility ($1/\chi$–T) curve (see the Supplemental Material [28]). Below T_C, the in-plane magnetization is observed much smaller than the out-of-plane one. Figure 2(b) shows in-plane and out-of-plane magnetization-field (M–H) hysteresis loops of the SMIO film measured at 10 K, exhibiting a saturated magnetization of approximately $0.80\mu_B$ per formula unit (approximately 120 emu cm^{-3}). In the out-of-plane direction, the magnetization saturates at approximately 0.5 T, while in the in-plane direction, the saturation occurs above 5 T. M–H loops and M–T curves reveal that the magnetic easy axis of the SMIO film is out of plane along [001]. In other words, the SMIO film exhibits a PMA, which is rare in oxide thin films due to the demagnetization effect that forces the magnetization lying in plane.
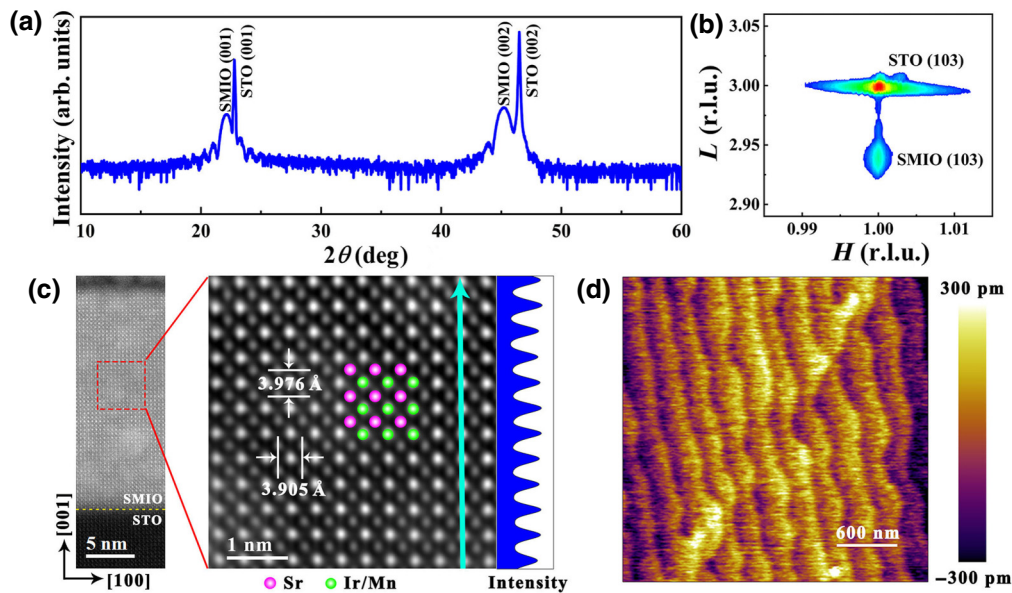

FIG. 1. (a) ω–2θ XRD pattern of the SMIO film deposited on (001) STO substrate; (b) reciprocal space mapping of the SMIO film around the (103) reflection of the STO substrate; (c) cross-section HAADF STEM images of the SMIO film recorded along the [010] zone axis. The right panel shows the intensity profile along the green arrows in (c); (d) surface morphology of the SMIO film.
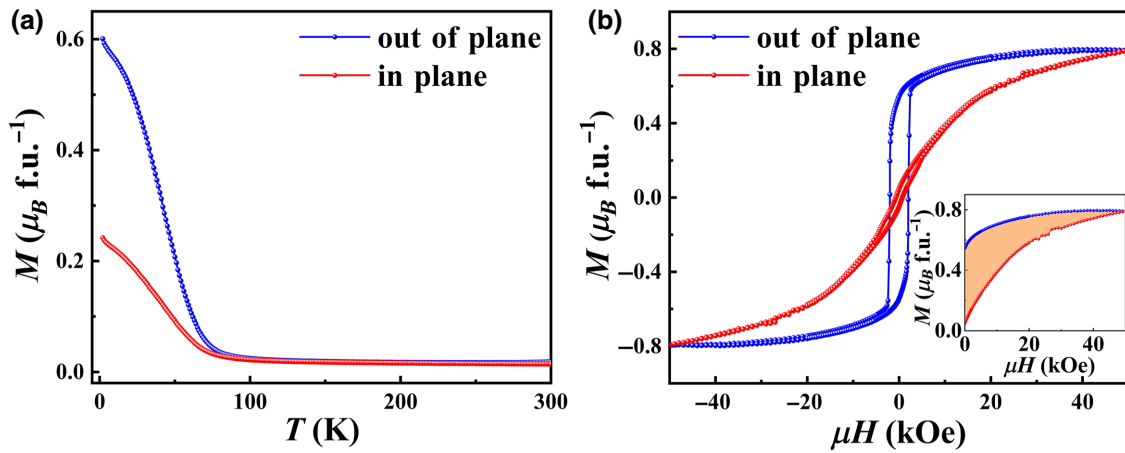
FIG. 2.   (a) Temperature dependence of in-plane (red) and out-of-plane (blue) magnetization of the SMIO film measured after cooling in 5-T field; (b) in-plane (red) and out-of-plane (blue) magnetization-field hysteresis loops of the SMIO film measured at 10 K; the inset shows schematically how K_{eff} is evaluated.

To quantify the PMA, an effective anisotropy constant K_{eff} is used, defined as the area enclosed between the out-of-plane and in-plane hysteresis loops, as shown in the inset of Fig. 2(b). By this definition, K_{eff} is positive when the magnetization is preferentially oriented perpendicular to the film plane. The direct calculation comes to a strong $K_{\text{eff}} \sim 1.2 \times 10^6$ erg cm^{-3} at 10 K for the SMIO film, comparable with that of the SrRuO$_3$ film, which is well known for its PMA with an anisotropic energy above 10^6 erg cm^{-3} [30]. *M–H* loops of the SMIO film are also measured at 30, 50, 70, and 100 K to obtain K_{eff} as a function of temperature, as shown in Fig. S3 within the Supplemental Material [28]. It is clear that PMA occurs in the ferromagnetic phase and K_{eff} decreases with increasing temperature, disappearing finally at T_C about 110 K. However, ferromagnetic LSMO thin films, frequently proposed for oxide spintronic devices, usually exhibit a negative K_{eff} with the Mn spins lying in plane [31]. Extensive efforts have been made to overcome the shape anisotropy in order to achieve PMA in the LSMO thin films. For example, Suzuki *et al*. deposited LSMO thin films on (001)-oriented LaAlO$_3$ substrates with a $K_{\text{eff}} \sim 8.4 \times 10^4$ erg cm^{-3}, an order of magnitude less than that of the SMIO film [32]. Interfacial couplings in artificial heterostructures were also employed. Han *et al*. studied the magnetic anisotropy of LSMO/YBaCo$_2$O$_{5+\delta}$ superlattices and reported an interfacial Mn—Co covalent bond induced PMA with a K_{eff} about 4.0×10^6 erg cm^{-3} [33]. Yi *et al*. reported that LSMO/SIO superlattices with desired microstructures may exhibit a K_{eff} about 1.5×10^6 erg cm^{-3} associated with the strong SOC of Ir at 10 K [12]. The giant PMA observed in simple SMIO films suggests that the SMIO films may have potential applications in high-density, low-power-consumption perovskite spintronic devices.

Figure 3(a) shows XPS measurements of the Mn 2p core level of SMIO at room temperature, in comparison with those of epitaxial LSMO film and SrMnO$_3$ (SMO) thin films deposited on (001)-oriented STO by pulsed-laser deposition. The SMO film shows a Mn 2p doublet at 641.5 and 653.1 eV with a spin-orbit split of about 11.6 eV, in agreement with previous reports of Mn^{4+} cations [34,35]. Both LSMO and SMIO thin films show much broader Mn 2p doublets with the 2$p_{3/2}$ peak at 640.3 eV for LSMO and 640.8 eV for SMIO, lower by 1.2 and 0.7 eV than that of SMO, respectively. This indicates that the Mn valence decreases from SMO to SMIO and further to LSMO films, which is known to have mixed Mn^{3+} and Mn^{4+} cations. By fitting the Mn 2p spectra of LSMO with multiple Lorentzian-Gaussian peaks, one may decompose the spectra into two 2$p_{3/2}$/2$p_{1/2}$ doublets, one at the same binding energies as those in SMO, i.e., 641.5 and 653.1 eV for Mn^{4+}, and the other at lower binding energies 640.1 and 651.6 eV for Mn^{3+} cations, according to previous reports [36,37]. The Mn^{3+}/Mn^{4+} atomic ratio in the LSMO film obtained from the fitting is about 64/36. Direct calculation of the average Mn valence comes to +3.36, in good agreement with the nominal Mn valence of +3.33 in LSMO. The Mn 2p spectra of SMIO can be well fitted with the same two spin-orbital doublets decomposed from the spectra of LSMO. The fitting generates a Mn^{3+}/Mn^{4+} atomic ratio of about 39/61, corresponding to an average Mn valence of about +3.61. Figure 3(b) shows the Ir 4f core-level XPS of the SMIO film, in comparison with that of a SIO film deposited on (001)-oriented STO by pulsed-laser deposition. The binding energy of Ir 4$f_{7/2}$/4$f_{5/2}$ spin-orbital doublet in SMIO appears at 62.6 and 65.5 eV, higher by 0.3 eV than those in SIO. This indicates that SMIO has mixed Ir^{4+} and Ir^{5+} cations, showing
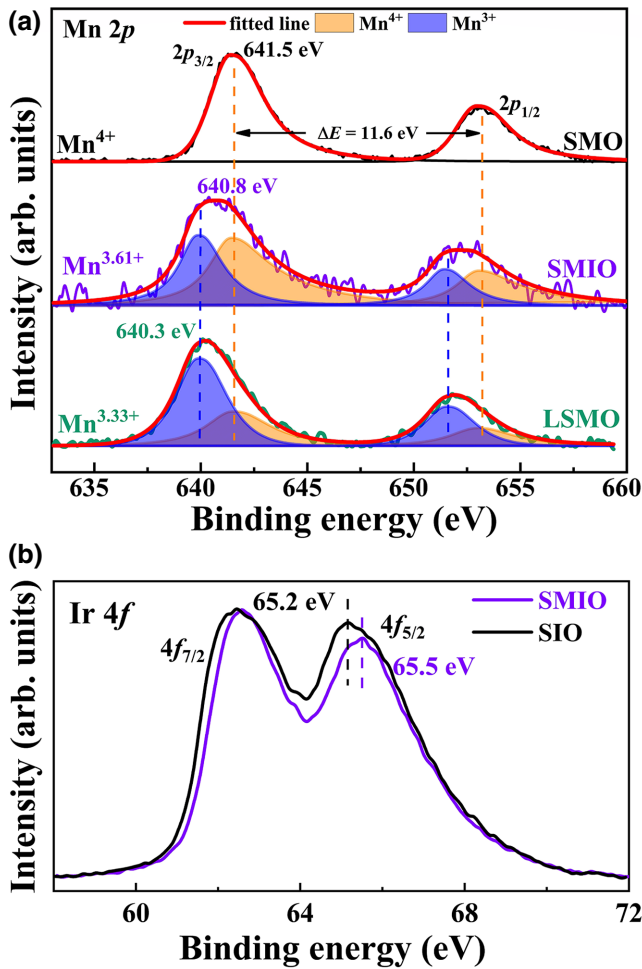
FIG. 3. XPS of Mn $2p$ (a) and Ir $4f$ (b) core levels of the SMIO film in comparison with SMO, LSMO, and SIO films, respectively, deposited on (001) STO substrates.

a higher average valence than +4 as in SIO. To keep neutral with the +3.61 Mn valence, the average Ir valence in the SMIO film can be calculated as +4.17. The valences of Mn and Ir observed here in the SMIO film are reasonable, because an electron transfer from Ir^{4+} $J_{eff}=1/2$ orbital to the empty Mn^{4+} e_g orbital has been frequently reported at the manganite/SIO interface [38,39].

Since Mn and Ir cations are uniformly distributed in the SMIO thin film, there are three kinds of possible nearest-neighbor exchange interactions mediated by O anions (i.e., Mn–O–Mn, Ir–O–Ir, and Ir–O–Mn). Furthermore, Mn cations are at +3.61 and Ir cations are at +4.17, obtained from the XPS measurement. It is well known that double exchange in mixed-valence Mn^{3+}–O–Mn^{4+} favors a parallel alignment of the Mn spins, as observed in a variety of doped manganites [40–42]. For Ir–O–Ir, the spin-orbital entangled half-filled $J_{eff}=1/2$ band renders the antiferromagnetic behavior observed in various Ir^{4+} perovskites, such as SIO and Sr_2IrO_4 [43–45]. However, in the

SMIO film with mixed-valence Ir^{4+}–O–Ir^{5+}, the double exchange interaction prefers parallel Ir moments, similar to the Mn^{3+}–O–Mn^{4+} [46]. Qasim *et al.* once reported a spin-glass behavior with short-range ferromagnetic interactions in Mg-doped SIO with a +4.5 Ir valence [47]. Nichols *et al.* have also reported a net Ir magnetic moment in SIO/SMO superlattices due to the mixed Ir valence and identified the dominant orbital contribution associated with strong SOC in Ir cations [38]. For Ir–O–Mn interactions in the SMIO film, it is reasonable that Ir and Mn moments are aligned antiparallel, as experimentally observed at the interface in many manganite/iridate heterostructures [38, 48]. The average Mn valence in the SMIO film is +3.61 estimated from the XPS results above, suggesting that each Mn provides a spin of approximately $3.40\mu_B$ [49]. Shapiro *et al.* have reported a moment approximately $0.33\mu_B$/Ir with +4 valence measured by neutron-powder-diffraction [50]. Nichols *et al.* have reported a moment $\sim 0.08\mu_B$/Ir with +4.50 valence measured by x-ray magnetic circular dichroism [38]. A rough estimation, assuming that the Ir moment decreases proportional to the increase of Ir valence and becomes zero at +5.00, gives an Ir moment of about $0.24\mu_B$/Ir for the +4.17 valence in the SMIO film, much smaller than the Mn contribution. Direct calculation comes to a magnetic moment of about $0.85\mu_B$ per formula unit in SMIO films, close to the experimental value.

C. Effects of lattice distortion

Lattice distortion is well known to have a great effect on the PMA of manganite thin films, since magnetic anisotropy is sensitive to the ligand field as functions of bond lengths and bond angles [51]. To elucidate whether and how the PMA observed in the SMIO film varies with lattice distortion, epitaxial SMIO thin films are deposited on BTO buffered (001)-oriented STO substrates with the same thickness as deposited on bare (001)-oriented STO substrate. Thin compressively strained BTO layers can be deposited coherently to the STO substrate lattice. But the BTO lattice partially relaxes when the layer thickness exceeds a critical value, below which the chemical energy gain compensates for the increase of the elastic energy [52–54]. By carefully controlling the BTO buffer layer thickness, a series of substrates with increasing in-plane lattice constants are achieved. The XRD patterns of these films exhibit a high crystalline quality with no observable secondary phases (see the Supplemental Material [28]). The thickness of all SMIO films are kept at about 20 nm. Figures 4(a)–4(c) show reciprocal space mappings around the (103) spot of STO for SMIO thin films deposited on 25-, 60-, and 80-nm-thick BTO buffer layers, respectively. It is observed that the (103) spot of BTO shifts toward upper left with increasing thickness, indicating the relaxation with increasing in-plane
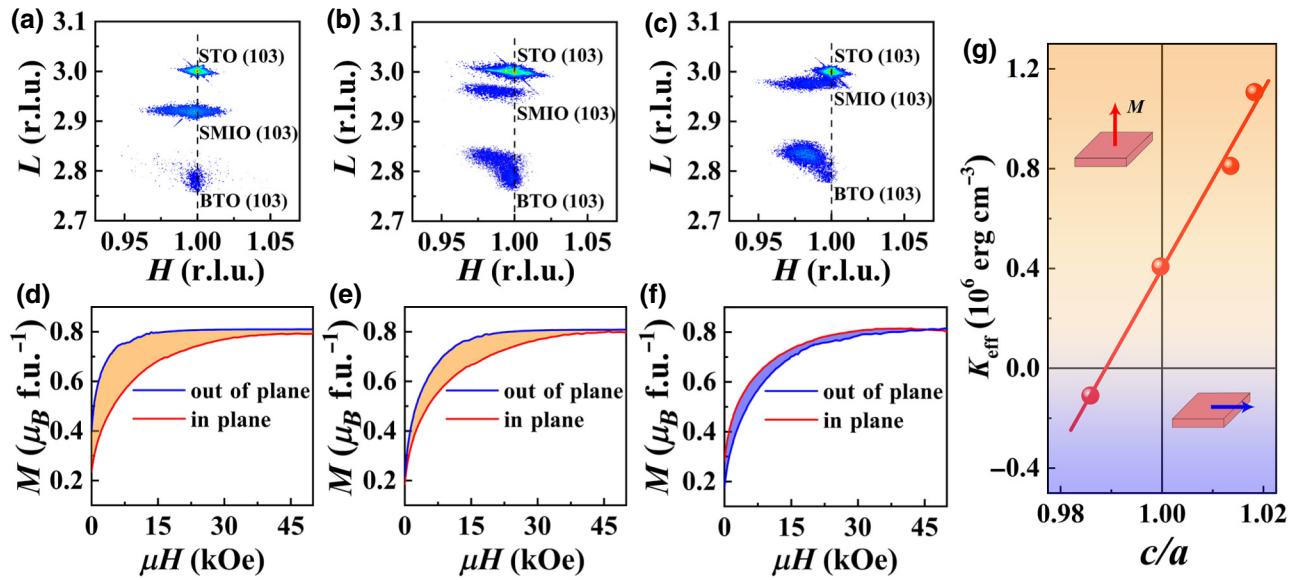
FIG. 4.   Reciprocal space mappings (a)–(c) around the (103) spot of SMIO/BTO heterostructures and corresponding in-plane (red) and out-of-plane (blue) magnetization-field hysteresis loops (d)–(f) measured at 10 K with 25- (a),(d), 60- (b),(e), and 80-nm- (c),(f) thick BTO buffer layers. (g) K_{eff} as a function of tetragonality.

but decreasing out-of-plane lattice constants, and that the (103) spot of each SMIO film shares the same in-plane reciprocal vector with that of BTO buffer, indicating that the SMIO films are coherent and fully strained to the BTO lattices. Accordingly, the tetragonality of the SMIO film decreases with increasing BTO buffer thickness, from 1.018 in absence of the buffer to 0.988 with the 80-nm-thick buffer. Note that the SMIO film deposited on the 60-nm-thick BTO buffer shows identical in-plane and out-of-plane lattice constants, generating $c/a = 1$, i.e., a cubic lattice. Cross-section HAADF STEM image of the SMIO film deposited on the 80-nm-thick BTO buffer layer demonstrates the coherent SMIO/BTO interface (see the Supplemental Material [28]). Figures 4(d)–4(f) show in-plane and out-of-plane M–H curves of the SMIO films deposited on 25-, 60-, and 80-nm-thick BTO buffer layers, respectively. It is clear that all the SMIO films show the same saturated magnetization of about $0.80\mu_B$ per formula unit. K_{eff}, as the area enclosed between the in-plane and out-of-plane M–H curves, are plotted as a function of SMIO tetragonality in Fig. 4(g). K_{eff} decreases linearly with the increase of BTO buffer thickness and the decrease of tetragonality, in agreement with previous results that PMA is enhanced in compressively strained manganites with a large c/a [30]. However, with $c/a = 1$ on the 60-nm-thick BTO buffer layer, the SMIO film still exhibits a positive K_{eff} of about 4.0×10^5 erg cm^{-3}. It is only when deposited on the 80 nm thick BTO buffer layer that the SMIO film with a tetragonality of 0.988 shows a negative K_{eff} of about -1.5×10^5 erg cm^{-3}, indicating an in-plane magnetic easy axis.

According to the Bruno model, in manganite films, preferential occupancy of the $d_{3z^2-r^2}$ ($d_{x^2-y^2}$) orbital leads to out-of-plane (in-plane) magnetic easy axis through SOC [55]. XAS is used to investigate the orbital occupation. The L_3 and L_2 edges originate from electron transition from $2p_{3/2}$ and $2p_{1/2}$ orbitals to the empty $3d$ orbitals, respectively. X-ray photons linearly polarized in-plane and out-of-plane excite electrons into different e_g orbitals. X-ray linear dichroism is defined as the difference between the absorption intensities to photons polarized in plane and out of plane. As is well documented, the integration of the XLD spectrum around the L_2 absorption peak gives a direct measure to the occupation of the e_g orbitals [56,57]. Negative (positive) value corresponds to a preferential occupancy of the $d_{x^2-y^2}$ ($d_{3z^2-r^2}$) orbital. Figure 5 shows normalized Mn L-edge XAS and corresponding XLD measured at 80 K for the SMIO film deposited on bare STO, and the 60- and 80-nm-thick BTO buffered STO, respectively. It is observed that the XLD are positive around the L_2 edge for the SMIO films with PMA, as shown in the bottom panel of Figs. 5(a) and 5(b), indicating preferential occupancy of the $d_{3z^2-r^2}$ orbital. Figure 5(c) shows that the XLD of the SMIO film deposited on the 80-nm-thick BTO buffer, which exhibits an in-plane magnetic easy axis, is negative as expected, corresponding to a preferential occupancy of the $d_{x^2-y^2}$ orbital. Figure 5(d) shows the XLD as a function of the SMIO tetragonality. The XLD value decreases with the increase of BTO buffer thickness and the decrease of tetragonality by an approximately linear relation, similar to the trend of K_{eff}, as shown in Fig. 4(g). The XLD measurement indicates that the observed PMA
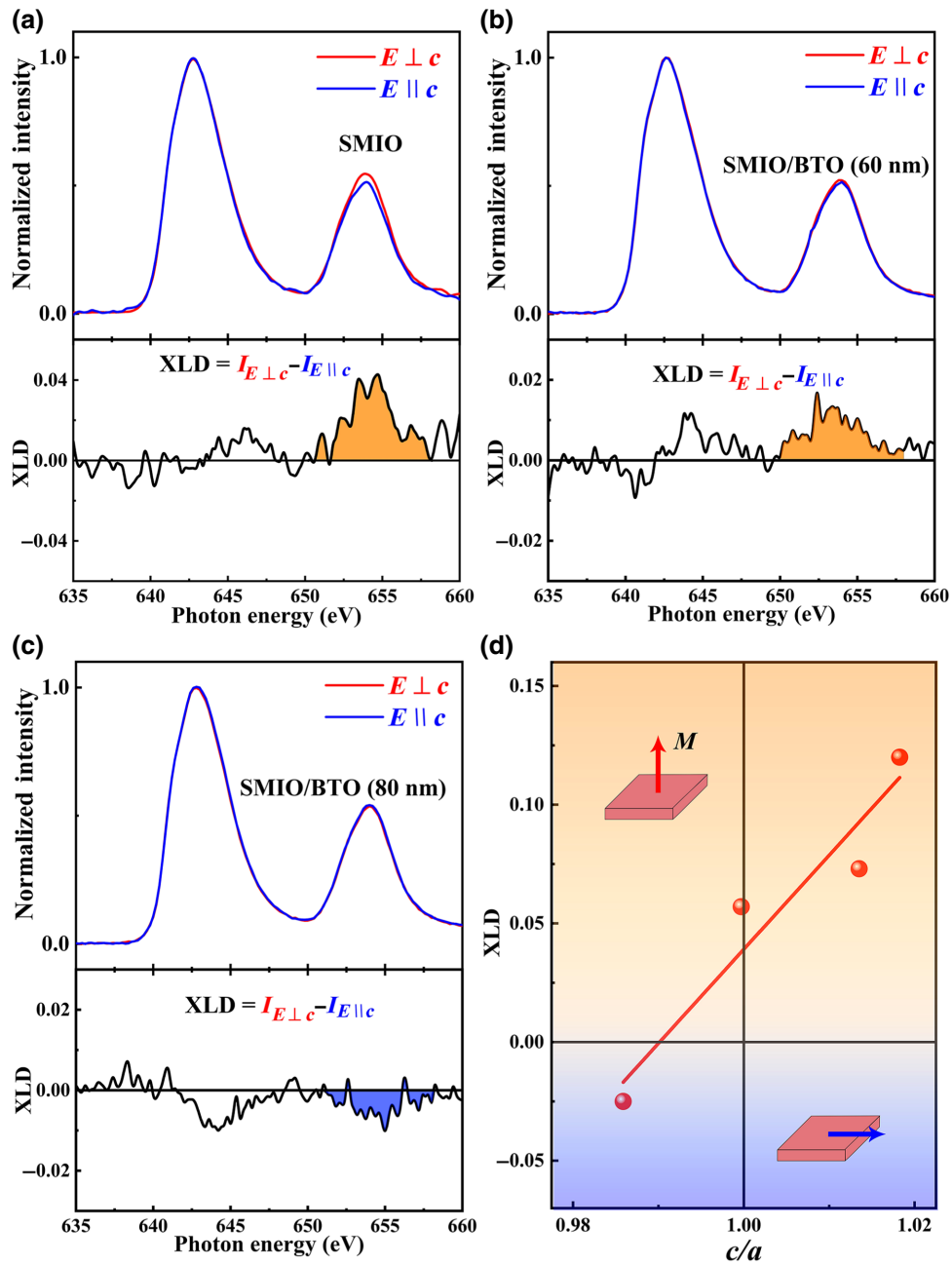
FIG. 5.   Normalized XAS spectra for the SMIO films deposited on bare STO (a) and 60- (b) and 80-nm- (c) thick BTO buffered STO, measured with photons polarized in-plane and out-of-plane, respectively. Bottom panels in (a)–(c) are the corresponding XLD spectra. (d) XLD, integrated around the L_2 edge from 650 to 658 eV, as a function of SMIO tetragonality.

in SMIO films is indeed correlated with the preferential occupancy of the Mn $d_{3z^2-r^2}$ orbital.

D. Discussions

In a tetragonal lattice with $c/a > 1$, the stronger in-plane crystal field drives the electrons to preferentially occupy the Mn $3d_{3z^2-r^2}$ orbital, in favor of PMA. And the PMA can only be observed as long as the tetragonality is strong enough to overwhelm the shape anisotropy that favors an in-plane magnetization. However, in SMIO thin films, it is more complex since there is still notable PMA observed even when $c/a = 1$. Oxygen octahedral rotation has been reported to be useful in tuning magnetic anisotropy in terms of bond angles [25,26]. We assume that K_{eff} can be divided into three parts as

$$K_{eff} = K_{shape} + K_{LD} + K_{OOR}, \qquad (1)$$

where K_{shape} is from shape anisotropy, K_{LD} from lattice distortion, and K_{OOR} from oxygen octahedral rotation.
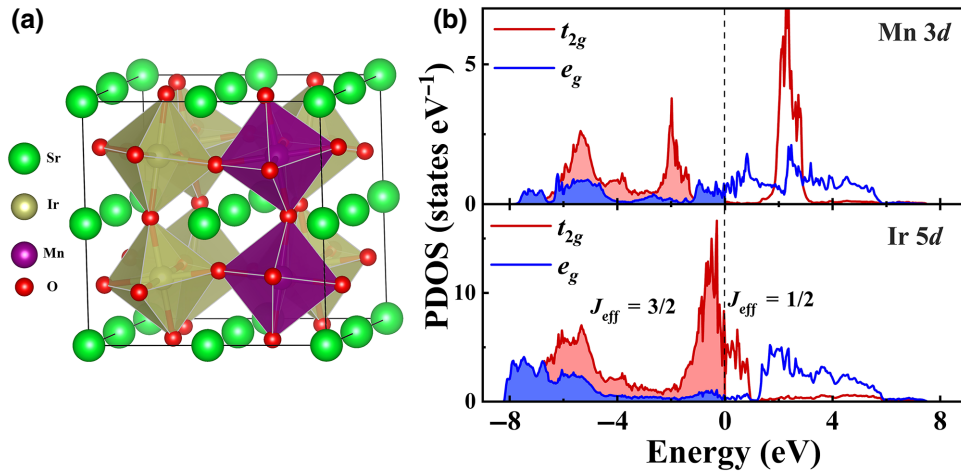
(a)

(b)

FIG. 6.   (a) Sketch of the SrMn$_{0.25}$Ir$_{0.75}$O$_3$ supercell for first-principles calculations with the two Mn cations as nearest neighbors; (b) PDOS of Mn 3d and Ir 5d orbitals from the calculations with SOC.

In SMIO thin films, K_{shape} is negative due to the shape anisotropy that favors an in-plane moment. As shown in Fig. S7 in the Supplementary Material [28], K_{eff} indeed decreases with decreasing SMIO film thickness from 20 to 5 nm. But the reduction in K_{eff} is very limited, indicating that K_{shape} does not play a dominant role. Therefore, it is reasonable to assume that SMIO films at the same thickness have the same K_{shape}. K_{LD}, as discussed above, depends on the anisotropy of crystal fields, which depends, in turn, on the lattice distortion, i.e., tetragonality. When $c/a = 1$, K_{LD} is assumed to be zero. The observed positive K_{eff} in the SMIO film with $c/a = 1$ suggests that K_{OOR} must be positive, which prefers a magnetic easy axis perpendicular to the film plane.

In order to get insight into the spin polarization of the Mn e_g orbitals, first-principles calculations are performed. For ease of modeling, we consider a supercell composed of $2 \times 2 \times 2$ ABO$_3$ perovskite unit cells with six Ir and two Mn on the perovskite B sites. The composition of the supercell, i.e., SrMn$_{0.25}$Ir$_{0.75}$O$_3$, is close to the SMIO film experimentally studied. In the calculations, three configurations of Ir and Mn cations are considered in line with the random distribution observed, as shown in Fig. 6(a) and in Fig. S6 within the Supplemental Material [28]. However, all the three distributions give similar results and we show only the results with the two Mn cations as the nearest neighbors in the supercell, as shown in Fig. 6(a). The results of the other two distributions are reported in Fig. S6 within the Supplemental Material [28]. Calculations show that the ground state of SMIO consists of parallel alignment of Ir moments, parallel alignment of Mn moments, but antiparallel alignment of Ir and Mn moments (see the Supplemental Material [28]). Figure 6(b) shows the projected density of states (PDOS) for Mn 3d orbitals in the top panel and Ir 5d in the bottom panel. For Mn 3d orbitals, the Fermi level crosses e_g states while the t_{2g} orbitals are

clearly split near the Fermi level, indicating that three d electrons occupied the three t_{2g} orbitals and the e_g orbitals are also partially occupied. This is consistent with the measured average Mn valence. For Ir 5d electrons, the t_{2g} orbitals split into orbitals of $J_{eff} = 3/2$ and $J_{eff} = 1/2$ due to the strong SOC. The e_g orbitals of Ir are also partially filled. Okamoto *et al.* have proposed that molecular orbitals form among e_g orbitals of neighboring Mn and Ir cations across the SMO/SIO interface and electrons transfer from the Ir $J_{eff} = 1/2$ orbital to the bonding molecular orbital [58]. Our calculations are in agreement with this molecular orbital scenario.

As calculations reveal that the SMIO perovskite structure adopts $\mathbf{a^- a^- c^+}$ oxygen octahedral rotation pattern (Glazer notation [59]), the effect of oxygen octahedral rotation on the orbital occupation in Mn e_g orbitals in the SIMO film when $c/a = 1$ are further investigated. The oxygen octahedral rotation angles around [100], [010], and [001] axes are calculated to be 8°, 8°, and 6°, respectively, for the supercell shown in Fig. 6(a). Figure 7(b) shows the Mn $d_{3z^2-r^2}$ and $d_{x^2-y^2}$ PDOS of the SMIO film with the $\mathbf{a^- a^- c^+}$ oxygen octahedral rotation pattern, and those decomposed into the $\mathbf{a^0 a^0 c^+}$ pattern with the 6° out-of-plane tilting and the $\mathbf{a^- a^- c^0}$ pattern with 8° in-plane tilting. It is observed that both $d_{3z^2-r^2}$ and $d_{x^2-y^2}$ orbitals are all partially occupied. The electron occupancy of $d_{3z^2-r^2}$ ($n_{d_{3z^2-r^2}}$) and $d_{x^2-y^2}$ orbitals ($n_{d_{x^2-y^2}}$) are calculated. The ratio $n_{d_{3z^2-r^2}} : n_{d_{x^2-y^2}}$ is 1.13:1, 1.17:1, and 1.02:1 for the $\mathbf{a^- a^- c^+}$, $\mathbf{a^0 a^0 c^+}$, and $\mathbf{a^- a^- c^0}$ pattern, respectively. The large occupancy ratio of the $\mathbf{a^0 a^0 c^+}$ pattern suggests that the out-of-plane octahedral rotation favors more occupancy of the $d_{3z^2-r^2}$ orbital. The oxygen octahedron rotation may result in the magnetic easy axis perpendicular to the film plane even in SMIO film with $c/a = 1$.
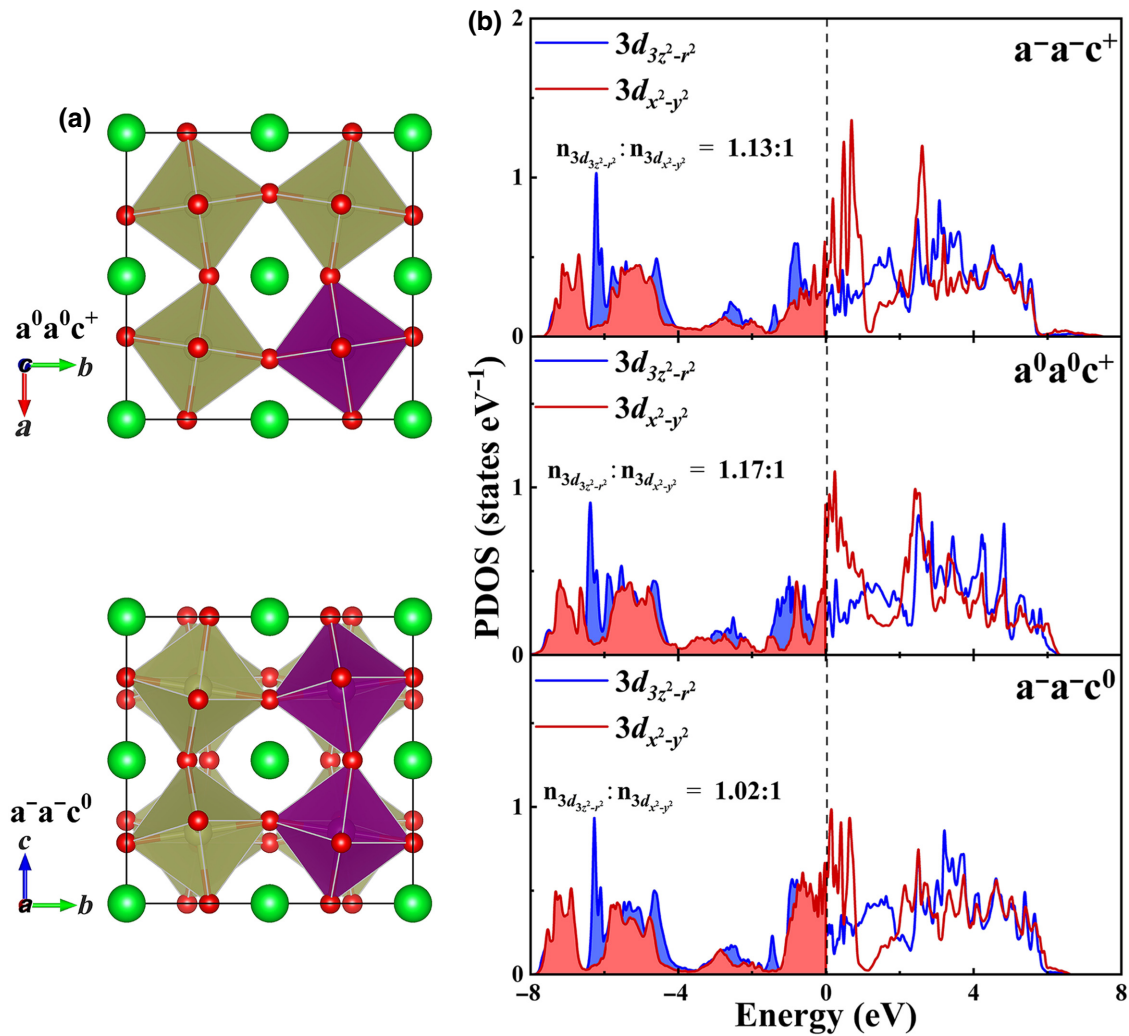
FIG. 7. (a) Sketch of structures with oxygen octahedral rotation pattern $\mathbf{a^0a^0c^+}$ and $\mathbf{a^-a^-c^0}$. (b) PDOS of Mn $3d$–e_g states with $\mathbf{a^-a^-c^+}$, $\mathbf{a^0a^0c^+}$, or $\mathbf{a^-a^-c^0}$. $d_{3z^2-r^2}$ and $d_{x^2-y^2}$ orbitals are marked in blue and red colors, respectively.

IV. CONCLUSION

In summary, magnetic characteristics of SMIO thin films epitaxially deposited on (001)-oriented STO substrates and BTO buffers by pulsed-laser deposition are studied systematically. Ferromagnetic behavior and strong PMA with a large effective anisotropy constant approximately 1.2×10^6 erg cm^{-3} at 10 K are observed. XPS measurements reveal a +3.61 valence state of Mn and +4.17 valence state of Ir. Mixed valence states of Mn and Ir cations account for the ferromagnetism. With the help of first-principles calculations, the magnetization is revealed to come from antiparallel coupling of Ir and Mn moments, which are aligned ferromagnetically for themselves. The origin of strong PMA is found to be the preferential occupancy of the Mn $d_{3z^2-r^2}$ orbital induced by anisotropy of the lattice distortion and the oxygen octahedron rotation, which is confirmed by XLD measurements and first-principles calculations. Our work provides

a perovskite system that may have potential applications in high-density, and low-power-consumption perovskite spintronic devices with strong PMA.

[1] M. Bibes, J. E. Villegas, and A. Barthélémy, Ultrathin oxide films and interfaces for electronics and spintronics, Adv. Phys. **60**, 5 (2011).

[2] L. Liu, Q. Qin, W. Lin, C. Li, Q. Xie, S. He, X. Shu, C. Zhou, Z. Lim, J. Yu, *et al.*, Current-induced magnetization switching in all-oxide heterostructures, Nat. Nanotechnol. **14**, 939 (2019).

[3] A. Manchon, H. C. Koo, J. Nitta, S. M. Frolov, and R. A. Duine, New perspectives for Rashba spin-orbit coupling, Nat. Mater. **14**, 871 (2015).

[4] Y. Li, L. Y. Zhang, Q. H. Zhang, C. Li, T. Y. Yang, Y. Deng, L. Gu, and D. Wu, Emergent topological Hall effect in La$_{0.7}$Sr$_{0.3}$MnO$_3$/SrIrO$_3$ heterostructures, ACS Appl. Mater. Interfaces **11**, 21268 (2019).

[5] S. Mangin, D. Ravelosona, J. A. Katine, M. J. Carey, B. D. Terris, and E. E. Fullerton, Current-induced magnetization reversal in nanopillars with perpendicular anisotropy, Nat. Mater. **5**, 210 (2006).

[6] S. Ikeda, K. Miura, H. Yamamoto, K. Mizunuma, H. D. Gan, M. Endo, S. Kanai, J. Hayakawa, F. Matsukura, and H. Ohno, A perpendicular-anisotropy CoFeB-MgO magnetic tunnel junction, Nat. Mater. **9**, 721 (2010).

[7] L. Q. Liu, C. F. Pai, Y. Li, H. W. Tseng, D. C. Ralph, and R. A. Buhrman, Spin-torque switching with the giant spin Hall effect of Tantalum, Science **336**, 555 (2012).

[8] S. Emori, U. Bauer, S. M. Ahn, E. Martinez, and G. S. D. Beach, Current-driven dynamics of chiral ferromagnetic domain walls, Nat. Mater. **12**, 611 (2013).

[9] N. Romming, C. Hanneken, M. Menzel, J. E. Bickel, B. Wolter, K. Bergmann, A. Kubetzka, and R. Wiesendanger, Writing and deleting single magnetic Skyrmions, Science **341**, 636 (2013).

[10] P. J. Hsu, A. Kubetzka, A. Finco, N. Romming, K. V. Bergmann, and R. Wiesendanger, Electric-field-driven switching of individual magnetic skyrmions, Nat. Nanotechnol. **12**, 123 (2017).

[11] R. D. Desautels, L. DeBeer-Schmitt, S. A. Montoya, J. A. Borchers, S. G. Je, N. Tang, M. Y. Im, M. R. Fitzsimmons, E. E. Fullerton, and D. A. Gilbert, Realization of ordered magnetic skyrmions in thin films at ambient conditions, Phys. Rev. Mater. **3**, 104406 (2019).

[12] D. Yi, H. Amari, P. P. Balakrishnan, C. Klewe, A. T. N'Diaye, P. Shafer, N. Browning, and Y. Suzuki, Enhanced Interface-Driven Perpendicular Magnetic Anisotropy by Symmetry Control in Oxide Superlattices, Phys. Rev. Appl. **15**, 024001 (2021).

[13] J. Zhang, F. Han, W. Wang, X. Shen, J. Zhang, H. Zhang, H. Huang, H. Zhang, X. Chen, S. Qi, *et al.*, Perpendicular magnetic anisotropy in La$_{1-x}$Sr$_x$CoO$_{2.5+\delta}$/La$_{2/3}$Sr$_{1/3}$MnO$_3$/La$_{1-x}$Sr$_x$CoO$_{2.5+\delta}$ trilayers ($x = 0.05$–0.5), Phys. Rev. B **100**, 094432 (2019).

[14] W. Lin, B. Yang, A. P. Chen, X. Wu, R. Guo, S. Chen, L. Liu, Q. Xie, X. Shu, Y. Hui, *et al.*, Perpendicular Magnetic Anisotropy and Dzyaloshinskii-Moriya Interaction at an Oxide/Ferromagnetic Metal Interface, Phys. Rev. Lett. **124**, 217202 (2020).

[15] J. Walter, S. Bose, M. Cabero, G. Yu, M. Greven, M. Varela, and C. Leighton, Perpendicular magnetic anisotropy via strain-engineered oxygen vacancy ordering in epitaxial La$_{1-x}$Sr$_x$CoO$_{3-\delta}$, Phys. Rev. Mater. **2**, 111404(R) (2018).

[16] Z. Guo, D. Lan, L. L. Qu, K. X. Zhang, F. Jin, B. B. Chen, S. W. Jin, G. Y. Gao, F. Chen, L. F. Wang, and W. B. Wu, Control of ferromagnetism and magnetic anisotropy via tunable electron correlation and spin-orbital coupling in La$_{0.67}$Ca$_{0.33}$MnO$_3$/Ca(Ir, Ru)O$_3$ superlattices, Appl. Phys. Lett. **113**, 231601 (2018).

[17] H. N. Peng, N. P. Lu, S. Z. Yang, Y. J. Lyu, Z. W. Liu, Y. F. Bu, S. C. Shen, M. Q. Li, Z. L. Li, L. Gao, *et al.*, A generic sacrificial layer for wide-range freestanding oxides with modulated magnetic anisotropy, Adv. Funct. Mater. **32**, 2111907 (2022).

[18] S. B. Hu, C. Cazorla, F. X. Xiang, H. F. Ma, J. Y. Wang, J. B. Wang, X. L. Wang, C. Ulrich, L. Chen, and J. Seidel, Strain control of giant magnetic anisotropy in metallic perovskite SrCoO$_{3-\delta}$ thin films, ACS Appl. Mater. Interfaces **10**, 22348 (2018).

[19] J. W. Kim, Y. Choi, J. Kim, J. F. Mitchell, G. Jackeli, M. Daghofer, J. van den Brink, G. Khaliullin, and B. J. Kim, Dimensionality Driven Spin-Flop Transition in Layered Iridates, Phys. Rev. Lett. **109**, 037204 (2012).

[20] S. Lin, Q. H. Zhang, M. A. Roldan, S. Das, T. Charlton, M. R. Fitzsimmons, Q. Jin, S. S. Li, Z. P. Wu, S. Chen, *et al.*, Switching Magnetic Anisotropy of SrRuO$_3$ by Capping-Layer-Induced Octahedral Distortion, Phys. Rev. Appl. **13**, 034033 (2020).

[21] Z. Lu, J. Liu, L. Wen, J. Feng, S. Kong, X. Zheng, S. Li, P. Jiang, Z. Zhong, J. Zhu, *et al.*, Lateral modulation of magnetic anisotropy in tricolor 3d-5d oxide superlattices, ACS Appl. Electron. Mater. **3**, 4210 (2021).

[22] D. Yi, J. Liu, S. L. Hsu, L. P. Zhang, Y. S. Choi, J. W. Kim, Z. H. Chen, J. D. Clarkson, C. R. Serrao, E. Arenholz, *et al.*, Atomic-scale control of magnetic anisotropy via novel spin-orbit coupling effect in La$_{2/3}$Sr$_{1/3}$MnO$_3$/SrIrO$_3$ superlattices, Proc. Natl. Acad. Sci. U. S. A. **113**, 6397 (2016).

[23] G. Kresse and J. Furthmüller, Efficient iterative schemes for *ab initio* total-energy calculations using a plane-wave basis set, Phys. Rev. B **54**, 11169 (1996).

[24] G. Kresse and J. Hafner, *Ab initio* molecular dynamics for liquid metals, Phys. Rev. B **47**, 558 (1993).

[25] Z. Liao, M. Huijben, Z. Zhong, N. Gauquelin, S. Macke, R. J. Green, S. Van Aert, J. Verbeeck, G. Van Tendeloo, K. Held, *et al.*, Controlled lateral anisotropy in correlated manganite heterostructures by interface-engineered oxygen octahedral coupling, Nat. Mater. **15**, 425 (2016).

[26] D. Kan, R. Aso, R. Sato, M. Haruta, H. Kurata, and Y. Shimakawa, Tuning magnetic anisotropy by interfacially engineering the oxygen coordination environment in a transition metal oxide, Nat. Mater. **15**, 432 (2016).

[27] J. P. Perdew, A. Ruzsinszky, G. I. Csonka, O. A. Vydrov, G. E. Scuseria, L. A. Constantin, X. Zhou, and K. Burke, Erratum: Restoring the Density-Gradient Expansion for Exchange in Solids and Surfaces, Phys. Rev. Lett. **100**, 136406 (2008).

[28] See Supplemental Material http://link.aps.org/supplemental/10.1103/PhysRevApplied.18.054083 for more details of structural and electronic state characterizations.

[29] M. Björck and G. Andersson, GenX: an extensible X-ray reflectivity refinement program utilizing differential evolution, J. Appl. Crystallogr. **40**, 1174 (2007).

[30] Z. X. Lu, Y. J. Yang, L. J. Wen, J. T. Feng, B. Lao, X. Zheng, S. Li, K. N. Zhao, B. S. Cao, Z. L. Ren, *et al.*, Cooperative control of perpendicular magnetic anisotropy via crystal structure and orientation in freestanding SrRuO$_3$ membranes, npj Flex. Electron. **6**, 9 (2022).

[31] Y. Wu, Y. Suzuki, U. Rüdiger, J. Yu, A. D. Kent, T. K. Nath, and C. B. Eom, Magnetotransport and magnetic domain structure in compressively strained colossal magnetoresistance films, Appl. Phys. Lett. **75**, 2295 (1999).

[32] Y. Suzukia, H. Y. Hwang, S. W. Cheong, T. Siegrist, R. B. van Dover, A. Asamitsu, and Y. Tokura, Magnetic anisotropy of doped manganite thin films and crystals, J. Appl. Phys. **83**, 7064 (1998).

[33] F. Han, X. Chen, J. Wang, X. Huang, J. Zhang, J. Song, B. Liu, Y. Chen, X. Bai, F. Hu, *et al.*, Perpendicular magnetic anisotropy induced by La$_{2/3}$Sr$_{1/3}$MnO$_3$-YBaCo$_2$O$_{5+\delta}$ interlayer coupling, J. Phys. D: Appl. Phys. **54**, 185302 (2021).

[34] G. C. Allen, S. J. Harris, J. A. Jutson, and J. M. Dyke, A study of a number of mixed transition metal oxide spinels using x-ray photoelectron spectroscopy, Appl. Surf. Sci. **37**, 111 (1989).

[35] B. J. Tan, K. J. Klabunde, and P. M. A. Sherwood, XPS studies of solvated metal atom dispersed (SMAD) catalysts. Evidence for layered cobalt-manganese particles on alumina and silica, J. Am. Chem. Soc. **113**, 855 (1991).

[36] L. Yin, C. B. Wang, L. Li, Q. Shen, and L. M. Zhang, Large room temperature magnetoresistance in La$_{0.9}$Sr$_{0.1}$MnO$_3$ thin films, J. Alloy. Compd. **730**, 327 (2018).

[37] Y. F. Chen, G. M. Wang, Z. F. Sun, S. G. Wang, Y. W. Mao, Q. R. Deng, and J. J. Yang, Magnetic characteristics of LaMnO$_{3+\delta}$ thin films deposited by RF magnetron sputtering in an O$_2$/Ar mixture gas, Mater. Res. Express **8**, 016101 (2021).

[38] J. Nichols, X. Gao, S. Lee, T. L. Meyer, J. W. Freeland, V. Lauter, D. Yi, J. Liu, D. Haskel, J. R. Petrie, *et al.*, Emerging magnetism and anomalous Hall effect in iridate–manganite heterostructures, Nat. Commun. **7**, 12721 (2014).

[39] Z. S. Lim, C. J. Li, Z. Huang, X. Chi, J. Zhou, S. W. Zeng, G. J. Omar, Y. P. Feng, A. Rusydi, S. J. Pennycook, *et al.*, Emergent topological Hall effect at a charge-transfer interface, Small **16**, 2004683 (2020).

[40] W. Niu, W. Q. Liu, M. Gu, Y. D. Chen, X. Q. Zhang, M. H. Zhang, Y. Q. Chen, J. Wang, J. Du, F. Q. Song, *et al.*, Emergent ferromagnetism: direct demonstration of the emergent magnetism resulting from the multivalence Mn in a LaMnO$_3$ epitaxial thin film system, Adv. Electron. Mater. **4**, 1800055 (2018).

[41] Y. Sun, X. J. Xu, W. Tong, and Y. H. Zhang, Double-exchange ferromagnetism and magnetoresistance in LaMn$_{1-x}$Cu$_x$O$_3$ ($x \leq 0.3$), Appl. Phys. Lett. **77**, 2734 (2000).

[42] G. M. Zhao, Double exchange and the cause of ferromagnetism in doped manganites, Phys. Rev. B **62**, 11639 (2000).

[43] M. A. Zeb and H. Y. Kee, Interplay between spin-orbit coupling and Hubbard interaction in SrIrO$_3$ and related *Pbnm* perovskite oxides, Phys. Rev. B **86**, 085149 (2012).

[44] B. J. Kim, H. Jin, S. J. Moon, J. Y. Kim, B. G. Park, C. S. Leem, J. Yu, T. W. Noh, C. Kim, S. J. Oh, *et al.*, Novel $J_{\text{eff}} = 1/2$ Mott State Induced by Relativistic Spin-Orbit Coupling in Sr$_2$IrO$_4$, Phys. Rev. Lett. **101**, 076402 (2008).

[45] K. K. Wolff, S. Agrestini, A. Tanaka, M. Jansen, and L. H. Tjeng, Comparative study of potentially $J_{\text{eff}} = 0$ ground state Iridium(V) in SrLaNiIrO$_6$, SrLaMgIrO$_6$, and SrLaZnIrO$_6$, Z. Anorg. Allg. Chem. **643**, 2095 (2017).

[46] W. K. Zhu, M. Wang, B. Seradjeh, F. Yang, and S. X. Zhang, Enhanced weak ferromagnetism and conductivity in hole-doped pyrochlore iridate Y$_2$Ir$_2$O$_7$, Phys. Rev. B **90**, 054419 (2014).

[47] I. Qasim, B. J. Kennedy, and M. Avdeev, Stabilising the orthorhombic perovskite structure in SrIrO$_3$ through chemical doping. Synthesis, structure and magnetic properties of SrIr$_{1-x}$Mg$_x$O$_3$ ($0.20 \leq x \geq 0.33$), J. Mater. Chem. A **1**, 13357 (2013).

[48] S. Bhowal and S. Satpathy, Electronic structure and anomalous Hall effect in the ferromagnetic 3d-5d superlattice SrMnO$_3$/SrIrO$_3$, Phys. Rev. B **99**, 245145 (2019).

[49] J. B. Goodenough, Theory of the role of covalence in the perovskite-type manganites [La, M(II)]MnO$_3$, Phys. Rev. **100**, 564 (1955).

[50] M. C. Shapiro, S. C. Riggs, M. B. Stone, C. R. de la Cruz, S. Chi, A. A. Podlesnyak, and I. R. Fisher, Structure and magnetic properties of the pyrochlore iridate Y$_2$Ir$_2$O$_7$, Phys. Rev. B **85**, 214434 (2012).

[51] M. Kobayashi, L. D. Anh, M. Suzuki, S. K. Takada, Y. Takeda, S. Fujimori, G. Shibata, A. Tanaka, M. Tanaka, S. Ohya, and A. Fujimori, Alternation of Magnetic Anisotropy Accompanied by Metal-Insulator Transition in Strained Ultrathin Manganite Heterostructures, Phys. Rev. Appl. **15**, 064019 (2021).

[52] T. Zhao, F. Chen, H. B. Lu, G. Z. Yang, and Z. H. Chen, Thickness and oxygen pressure dependent structural characteristics of BaTiO$_3$ thin films grown by laser molecular beam epitaxy, J. Appl. Phys. **87**, 7442 (2000).

[53] K. Terai, M. Lippmaa, P. Ahmet, T. Chikyow, T. Fujii, H. Koinuma, and M. Kawasaki, In-plane lattice constant tuning of an oxide substrate with Ba$_{1-x}$Sr$_x$TiO$_3$ and BaTiO$_3$ buffer layers, Appl. Phys. Lett. **80**, 4437 (2002).

[54] H. Terauchi, Y. Watanabe, H. Kasatani, K. Kamagaki, Y. Yano, T. Terashima, and Y. Bando, Structural study of epitaxial BaTiO$_3$ crystals, J. Phys. Soc. Jpn. **61**, 2194 (1992).

[55] P. Bruno, Tight-binding approach to the orbital magnetic moment and magnetocrystalline anisotropy of transition-metal monolayers, Phys. Rev. B **39**, 865 (1989).

[56] F. M. F. de Groot, J. C. Fuggle, B. T. Thole, and G. A. Sawatzky, $L_{2,3}$ x-ray-absorption edges of d^0 compounds: K$^+$, Ca^{2+}, Sc^{3+}, and Ti^{4+} in O_h (octahedral) symmetry, Phys. Rev. B **41**, 928 (1990).

[57] D. Pesquera, G. Herranz, A. Barla, E. Pellegrin, F. Bondino, E. Magnano, F. Sánchez, and J. Fontcuberta, Surface symmetry-breaking and strain effects on orbital occupancy in transition metal perovskite epitaxial films, Nat. Commun. **3**, 1189 (2012).

[58] S. Okamoto, J. Nichols, C. Sohn, S. Y. Kim, T. W. Noh, and H. N. Lee, Charge transfer in Iridate-Manganite superlattices, Nano Lett. **17**, 2126 (2017).

[59] A. Glazer, The classification of tilted octahedra in perovskites, Acta Crystallogr. Sect. B **28**, 3384 (1972).